

## Article

# Improvement in Torque Density by Ferrofluid Injection into Magnet Tolerance of Interior Permanent Magnet Synchronous Motor <sup>†</sup>

In-Jun Yang <sup>1</sup>, Si-Woo Song <sup>1</sup>, Dong-Ho Kim <sup>1</sup>, Kwang-Soo Kim <sup>2</sup> and Won-Ho Kim <sup>3,\*</sup>

<sup>1</sup> Department of Electrical Engineering, Hanyang University, Seoul 04763, Korea; dlswns78@naver.com (I.-J.Y.); thdtldn93@naver.com (S.-W.S.); dongho500@naver.com (D.-H.K.)

<sup>2</sup> Department of Mechatronics Engineering, Halla University, Wonju 26404, Korea; kwangsoo2.kim@halla.ac.kr

<sup>3</sup> Department of Electrical Engineering, Gachon University, Seongnam 13120, Korea

\* Correspondence: wh15@gachon.ac.kr; Tel.: +82-31-750-5881

<sup>†</sup> This paper is an extended version of our paper published in 2020 IEEE Energy Conversion Congress and Exposition (ECCE), Detroit, MI, USA, 11–15 October 2020.

**Abstract:** In an interior permanent magnet synchronous motor, an adhesive such as bond is generally injected into the magnet tolerance to prevent vibration of the permanent magnet within the insertion space. In this case, a disadvantage is that the magnet tolerance does not contribute to the performance. In this paper, ferrofluid is inserted to improve the torque density, utilizing the magnet tolerance. When inserting ferrofluid into the magnet tolerance, it is important to fix the magnet because conventional adhesives are not used, and it is important that the ferrofluid does not act as a leakage path within the insertion space. In this study, a new rotor configuration using a plastic barrier that satisfies these considerations was introduced. The analysis was conducted through finite element analysis (FEA), and this technique was verified by comparing the simulation results and the experimental results through a dynamo test. It was confirmed that the no-load back electromotive force in the final model increased through ferrofluid injection.

**Keywords:** permanent magnet (PM) motor; interior permanent magnet synchronous motor (IPMSM); ferrofluid; torque density; magnet tolerance



**Citation:** Yang, I.-J.; Song, S.-W.; Kim, D.-H.; Kim, K.-S.; Kim, W.-H. Improvement in Torque Density by Ferrofluid Injection into Magnet Tolerance of Interior Permanent Magnet Synchronous Motor. *Energies* **2021**, *14*, 1736. <https://doi.org/10.3390/en14061736>

Academic Editor: Florin Nicolae Jurca

Received: 22 February 2021

Accepted: 17 March 2021

Published: 21 March 2021

**Publisher's Note:** MDPI stays neutral with regard to jurisdictional claims in published maps and institutional affiliations.



**Copyright:** © 2021 by the authors. Licensee MDPI, Basel, Switzerland. This article is an open access article distributed under the terms and conditions of the Creative Commons Attribution (CC BY) license (<https://creativecommons.org/licenses/by/4.0/>).

## 1. Introduction

When inserting a permanent magnet into the rotor core of an interior permanent magnet synchronous motor (IPMSM), it is ideal to match the insertion space and the size of the magnet. If the sizes of the insertion space and the magnet are the same, it is difficult to insert the magnet, so a magnet tolerance, a kind of empty space between the rotor core and the magnet, is necessary. When the size of the magnet tolerance is increased, the electromagnetic performance deteriorates. In addition, the magnet is broken due to vibration generated between the magnet and the magnet tolerance when the motor is operated at high speed. In order to prevent vibration between the magnet and the magnet tolerance, an adhesive is put into the magnet tolerance to fix the magnet. In this case, the magnet tolerance does not contribute to the performance improvement.

In this paper, ferrofluid is inserted to improve the torque density, utilizing the magnet tolerance. Various studies have been conducted on special materials including nanoparticles [1–8]. Ferrofluid is a magnetic liquid and refers to water or oil mixed with ultra-fine powder [9–16]. A photo of ferrofluid observed by transmission electron microscopy (TEM) is shown in Figure 1 [12]. Ferrofluid does not have magnetism when there is no magnetic field, but it becomes magnetized when an external magnetic field is applied with a magnet [9–16]. Substances with these properties are called superparamagnetic. Figure 2 shows the B-H curve of vacuum and ferrofluid [17]. In the B-H curve, the slope of the graph is the

permeability, and Figure 2 shows that the permeability of ferrofluid is much higher than that of the vacuum. Therefore, when ferrofluid is injected into the magnet tolerance, it can reduce the reluctance of the magnet tolerance and increase the electromagnetic performance by replacing the rotor core.

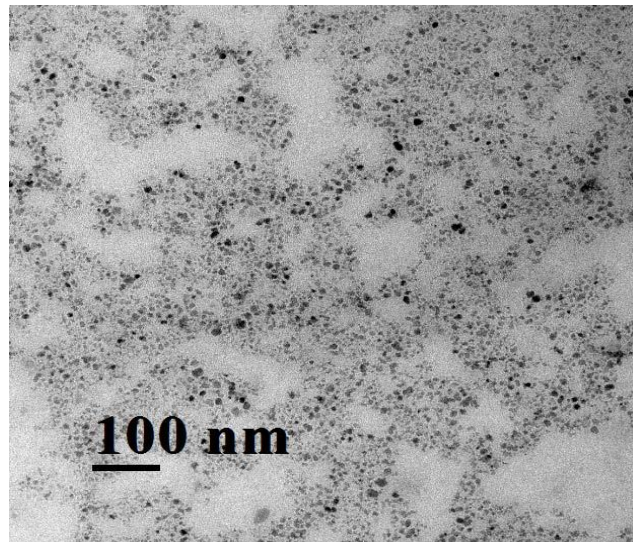


Figure 1. TEM image of  $Mn_{0.75}Zn_{0.25}Fe_2O_4$  (MZF) ferrofluid.

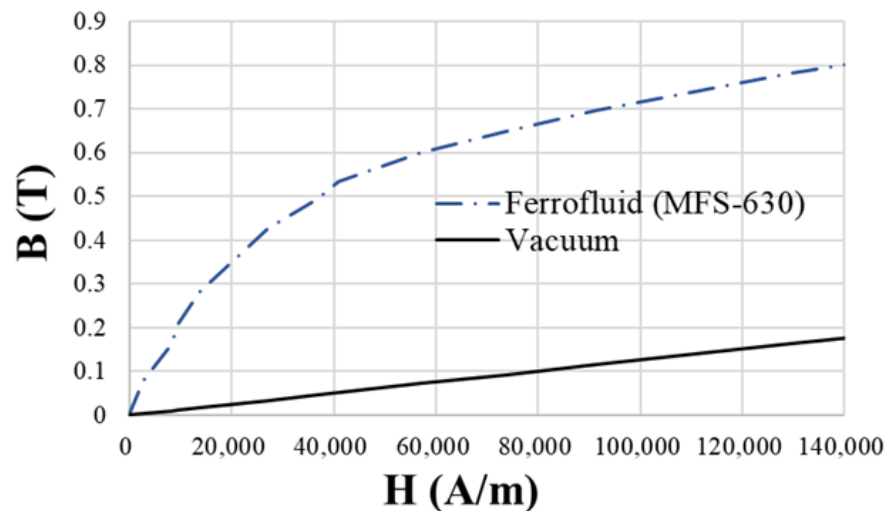


Figure 2. B-H curves of vacuum and ferrofluid.

There have been studies applying ferrofluid to increase electromagnetic performance in a motor. In Ref. [18], the motor was simplified, and the magnetic field and torque were calculated by applying ferrofluid. In [19,20], the force of the motor was calculated according to the saturation flux density by applying ferrofluid to the airgap of the stepping motor and the induction motor. Similarly, in Ref. [21], ferrofluid was applied to the airgap of the induction motor, and the effect of the viscosity of the ferrofluid was also analyzed. In all of the papers mentioned above, ferrofluid was applied to the airgap of a motor, and no study has applied ferrofluid to the magnet tolerance.

There are disadvantages to applying ferrofluid to the airgap as in Refs. [18–21]. Since particles of ferrofluid are not all insulated, eddy current loss occurs largely in areas with large changes in magnetic field. Using the airgap is greatly disadvantageous in terms of eddy current loss because the change in airgap flux density is much greater than that in the magnet tolerance located on either side of the magnet. In addition, sealing is very difficult.

Since the airgap is located between the rotating part and the fixed part, it is difficult to prevent the ferrofluid from escaping in the z-axis direction of the motor. On the contrary, it is quite advantageous in a mechanical design to insert the ferrofluid into the magnetic tolerance because a plastic air dummy can be used as a sealing cap by covering both ends of the z-axis of the rotor. In addition, a problem with using the airgap is the cost of ferrofluid. Ferrofluid is expensive compared to its capacity, and the price varies widely according to characteristics such as permeability and viscosity. Since the area of the airgap is much larger than that of the magnet tolerance, the capacity that can use ferrofluid also increases, which makes using the airgap quite disadvantageous in terms of cost. Finally, there is a problem of leakage flux. When ferrofluid is applied to the airgap, the magnetic flux of the magnet does not always return to the rotor through the stator [22]. In some cases, it comes directly back to the rotor through the ferrofluid of the airgap, and there is no way to control this [22]. When ferrofluid is applied to the magnet tolerance, on the other hand, it is possible to control the leakage flux through the rotor shape with minimal ferrofluid.

When inserting the ferrofluid into the magnet tolerance, it is important to fix the magnet because the existing adhesive is not used, and it is important that the ferrofluid does not act as a leakage path within the insertion space. In this study, a new rotor configuration that utilizes plastic barriers is proposed. The plastic barrier is a shape that wraps a permanent magnet at both ends within the insertion space. The plastic barrier prevents the ferrofluid from acting as a leakage flux path within the magnet tolerance and prevents the magnet from vibrating within the insertion space by fixing the magnet on both sides. It is also possible to minimize ferrofluid usage in the insertion space and increase the no-load back electromotive force (EMF). Finally, since the plastic barrier is shaped to fix the permanent magnet, the variable for the radial position of the permanent magnet can be selected. The model with the maximum no-load back EMF was selected by setting the length of the plastic barrier and the position of the magnet according to the radial direction as rotor variables. A model with the maximum no-load back EMF was chosen as the proposed model.

When designing the rotor by injecting ferrofluid, the no-load back EMF increases. It causes an increase not only in the magnetic torque and efficiency but also in the vibration and noise [23–26]. In order to design a high-performance and high-efficiency motor, it is necessary to consider vibration and noise, as well as the electromagnetic performance [23–26]. Therefore, a rotor design for decreasing vibration was additionally carried out with the proposed model [27–30].

The analysis model was selected as a 6-pole 9-slot IPMSM that enters the four-wheel drive (4WD) hydraulic control system, and the model that satisfied the target specifications through finite element analysis (FEA) was selected as the final model. A dynamo test for the prototype of the final model was conducted to compare the no-load line voltage according to the presence or absence of ferrofluid, and the test results were compared with the results of FEA to confirm the validity.

## 2. Magnetic Circuit through Ferrofluid Injection

Figure 3a shows the magnetic circuit for the half pole pair of IPMSM to obtain the magnetic flux of the airgap [22]. Using the motor's symmetry, the magnetic circuit for the 1-pole model, as shown in Figure 3a, was derived. The magnetic flux of the airgap determines the no-load back EMF and magnetic torque, which are measures of motor performance.

$R_s$  is the reluctance of the stator core, and  $2R_g$  is the reluctance of the airgap to half the magnet.  $R_{ls}$  is the reluctance of the magnetic flux that leaks to the adjacent pole without linking the armature winding, and  $R_{lb}$  is the reluctance for the magnetic flux that leaks to the adjacent pole through the barrier.  $R_t$  is the reluctance of magnet tolerance,  $2R_m$  is the reluctance for half the permanent magnet, and  $R_r$  is the reluctance of the rotor core. The magnetic flux that leaks into the rib is expressed as  $\Phi_{rib}$ , and this is considered in the permanent magnet source  $\Phi_r$ .  $\Phi_m$  is the magnetic flux leaving the permanent magnet;  $\Phi_{lb}$

is the leakage flux of the barrier.  $\Phi_m$  minus  $\Phi_{lb}$  is  $\Phi_{ma}$ .  $\Phi_{ls}$  is the leakage magnetic flux of the airgap, and  $\Phi_g$  is the magnetic flux of the airgap.

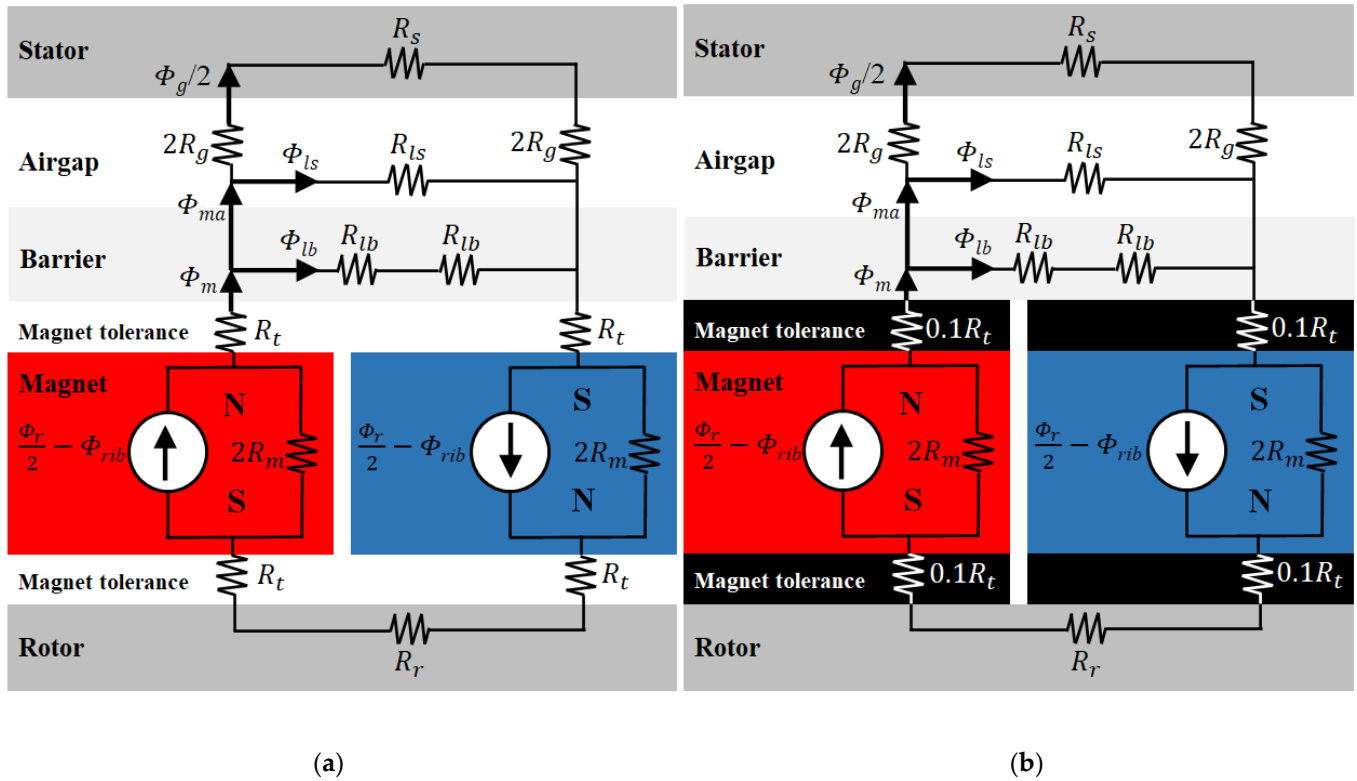


**Figure 3.** Magnetic circuit for the half pole pair of the interior permanent magnet synchronous motor (IPMSM): (a) conventional model; (b) conventional model with ferrofluid.

Figure 3b shows the magnetic circuit when ferrofluid is injected into the conventional model. Since the permeability of ferrofluid is 10 times larger than that of vacuum, it is possible to minimize the reluctance of the magnetic tolerance  $R_t$  through the injection of ferrofluid. The formula for reluctance can be expressed as follows. Therefore, in Figure 3b, the reluctance of the magnet tolerance is expressed as  $0.1R_t$ .

$$R = \frac{l}{\mu A} \tag{1}$$

The parallel circuit for  $R_{lb}$  and  $R_{ls}$  can be eliminated by using  $k_{lb}$ , the barrier leakage factor, and  $k_{ls}$ , the airgap leakage factor in Figure 3a. Those leakage factors have values slightly less than 1.  $\Phi_r$  and  $\Phi_{ma}$  can be expressed through the leakage factor as follows, which can lead to the expression of  $\Phi_g$ .

$$\phi_g = 2k_{ls}\phi_{ma} \tag{2}$$

$$\phi_{ma} = k_{lb}\phi_m \tag{3}$$

$$\phi_g = 2k_{lb}k_{ls}\phi_m \tag{4}$$

When the parallel circuit is removed through the leakage factor, the reluctance of the airgap, the rotor and stator, and the magnet tolerance is connected in series and is expressed as Equation (5). Here,  $k_r$  means the reluctance factor and has a value between 1 and 1.2.

$$4R_g + 4R_t + R_s + R_r = 4k_r R_g \tag{5}$$

The magnetic circuit of Figure 3a can be simply expressed as Figure 4a, and  $\Phi_m$  and  $\Phi_g$  of the conventional model are as follows:

$$\phi_m = \frac{1}{1 + k_r \frac{R_g}{R_m}} \left( \frac{\phi_r}{2} - \phi_{rib} \right) \quad (6)$$

$$\phi_g = \frac{2k_{lb}k_{ls}}{1 + k_r \frac{R_g}{R_m}} \left( \frac{\phi_r}{2} - \phi_{rib} \right) \quad (7)$$

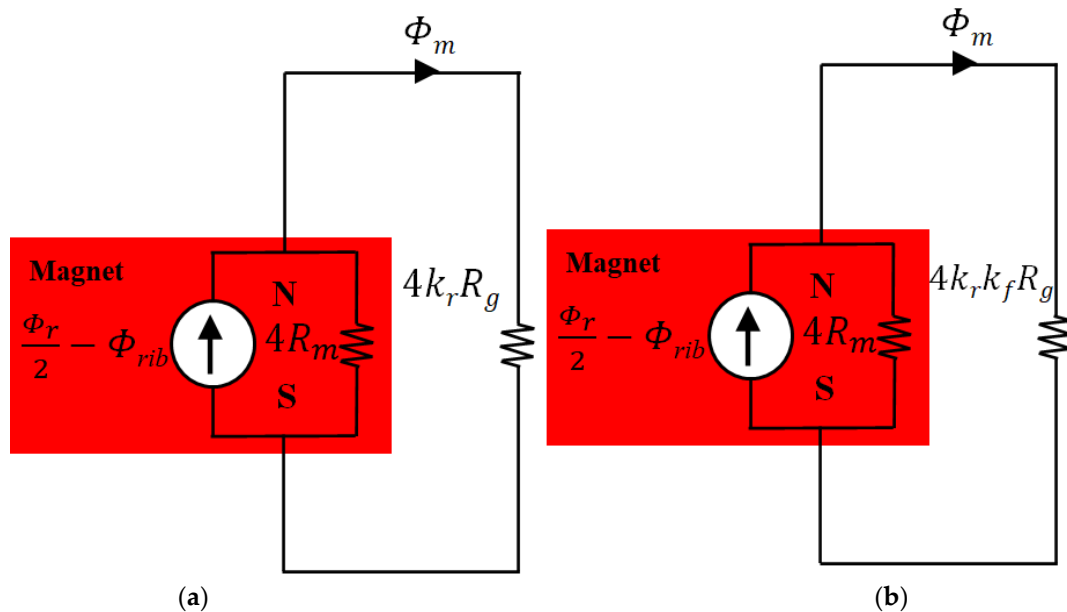


**Figure 4.** Simplification of magnetic circuit: (a) conventional model; (b) conventional model with ferrofluid.

The magnetic circuit of Figure 3b can be expressed as Figure 4b, and since the reluctance of the magnet tolerance is minimized, Equation (5) is expressed as follows:

$$4R_g + 0.4R_t + R_s + R_r = 4k_r k_f R_g \quad (8)$$

Here,  $k_f$  means the ferrofluid factor and represents a value between 0.9 and 1. Equation (7), which shows the airgap magnetic flux  $\Phi_g$  through the magnetic circuit of Figure 4b, is expressed as follows:

$$\phi_g = \frac{2k_{lb}k_{ls}}{1 + k_r k_f \frac{R_g}{R_m}} \left( \frac{\phi_r}{2} - \phi_{rib} \right) \quad (9)$$

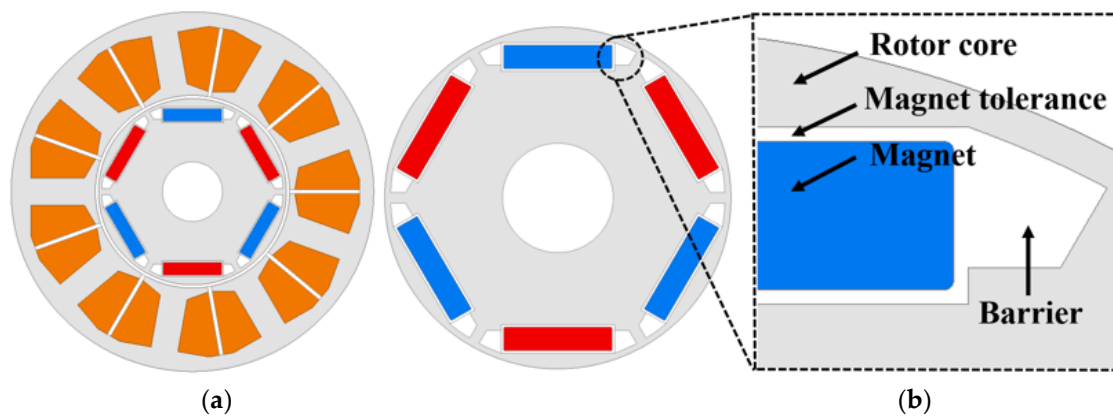
Equation (9) is larger than Equation (7), the airgap magnetic flux of the conventional model, due to the ferrofluid factor  $k_f$ . This means that the no-load back EMF and magnetic torque can be increased through ferrofluid injection.

### 3. Basic Design of Proposed Model

In order to confirm the performance improvement through ferrofluid injection, this section derives a model with the maximum no-load back EMF through FEA. To apply ferrofluid to a small motor with a large magnet tolerance compared to the size of a permanent magnet, IPMSM with a stator diameter of 56 mm was selected as the analysis model for a 4WD hydraulic control system. The specifications of the analysis model are shown in Table 1, and the cross-section of the full model and the rotor are respectively shown in Figure 5a,b. In general, the magnet tolerance is designed to be about 0.1 mm, but in this study, it was designed to be 0.2 mm to clearly confirm the change in performance for ferrofluid.

**Table 1.** Specifications of the analysis model.

Parameter	Value	Unit
Number of poles	6	-
Number of slots	9	-
Current	50	A <sub>peak</sub>
Rotating speed	4000	rpm
Stator outer/inner diameter	56/30	mm
Rotor outer/inner diameter	29/9.28	mm
Stator and rotor material	50PN470	-
Airgap length	0.5	mm
Stack length	38	mm
Magnet tolerance	0.2	mm
Magnet length and width	9.1/2	mm
Magnet material	N40SH	-
Number of turns	6	-

**Figure 5.** Cross-section of the conventional model: (a) full model; (b) rotor.

### 3.1. Rotor Design through Ferrofluid Injection

Figure 5b shows the conventional model without ferrofluid injection. Figure 6 is the shape of the rotor of a conventional model in which ferrofluid is injected into the magnet tolerance. Since the ferrofluid leaks into the barrier and the permanent magnet is not fixed, Figure 6 cannot actually be manufactured.

Figure 7 shows the waveform of the no-load back EMF, the standard for magnetic torque. Figure 7a,b show the case where the magnet tolerance is 0.1 mm and 0.2 mm, respectively. In Figure 7a, it can be seen that the  $V_{rms}$  value of the no-load back EMF increased by 6.56% through the injection of ferrofluid into the conventional model. In Figure 7b, since the amount of ferrofluid entering the magnet tolerance increases, the increase in the no-load back EMF is about 12.82%, and it can be seen that the increase in the no-load back EMF is about twice that of Figure 7a.

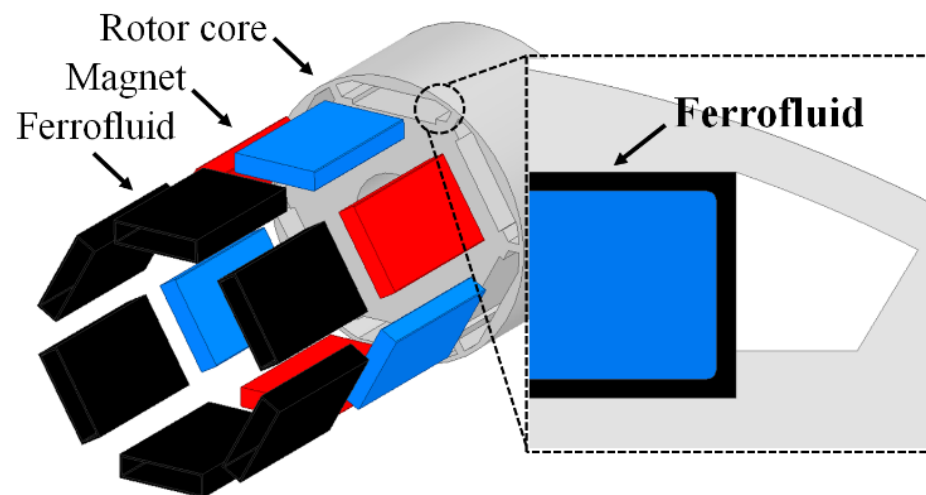


Figure 6. Rotor of the conventional model with ferrofluid.

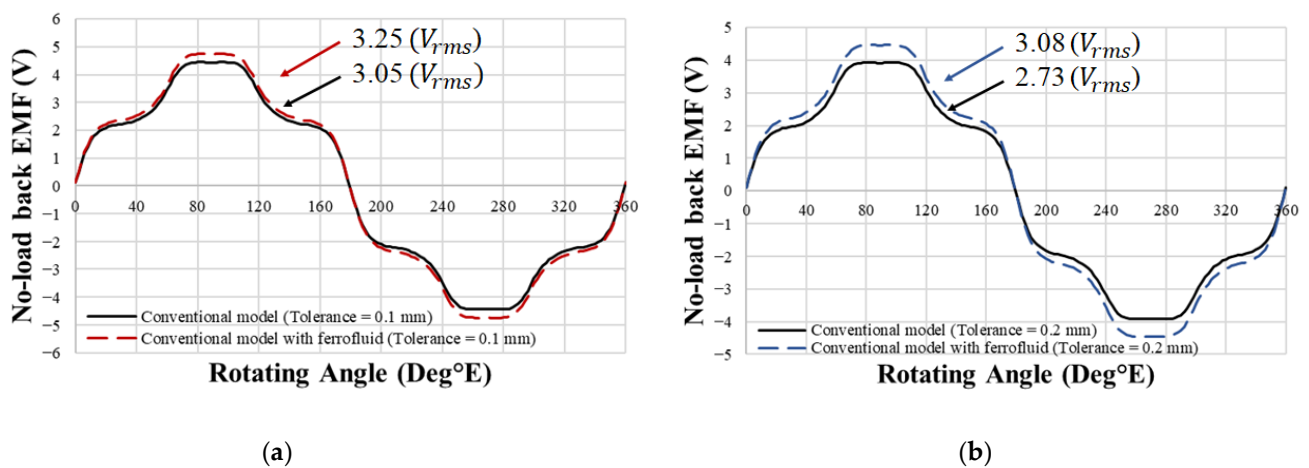


Figure 7. No-load back electromotive force (EMF) analysis (4000 rpm): (a) magnet tolerance = 0.1 mm; (b) magnet tolerance = 0.2 mm.

### 3.2. Selection of Rotor Variable and Proposed Model

As shown in Figure 6, when ferrofluid is injected into the magnet tolerance of the conventional model, the disadvantages are that the ferrofluid acts as a leakage flux path and cannot fix the permanent magnet, as shown in Figure 8a.

Figure 8b shows the rotor parameters. As shown in Figure 8b, by setting the barrier length  $D_{barrier}$  as a design variable, the barrier can be made into a shape that fixes the permanent magnets on both sides. If a nonmagnetic material such as plastic is injected into the barrier, it is possible to fix the permanent magnet and minimize the leakage magnetic flux path shown in Figure 8a. As the permanent magnet is fixed through the plastic barrier, it becomes possible to select  $D_{mag}$ , the position of the permanent magnet according to the radial direction, as a variable. Then, the model with the maximum no-load back EMF can be selected.

Figure 9 shows the analysis result of the no-load back EMF according to  $D_{barrier}$ . As the value of  $D_{barrier}$  increases, the leakage magnetic flux decreases and the back EMF increases. However, if the  $D_{barrier}$  becomes greater than 0.3 mm, the amount of ferrofluid unnecessarily decreases, even if the leakage magnetic flux path is minimized. As the no-load back EMF decreases when the amount of ferrofluid used is reduced, it is important to select the length of the  $D_{barrier}$  as the minimum length that can block the leakage magnetic flux path.

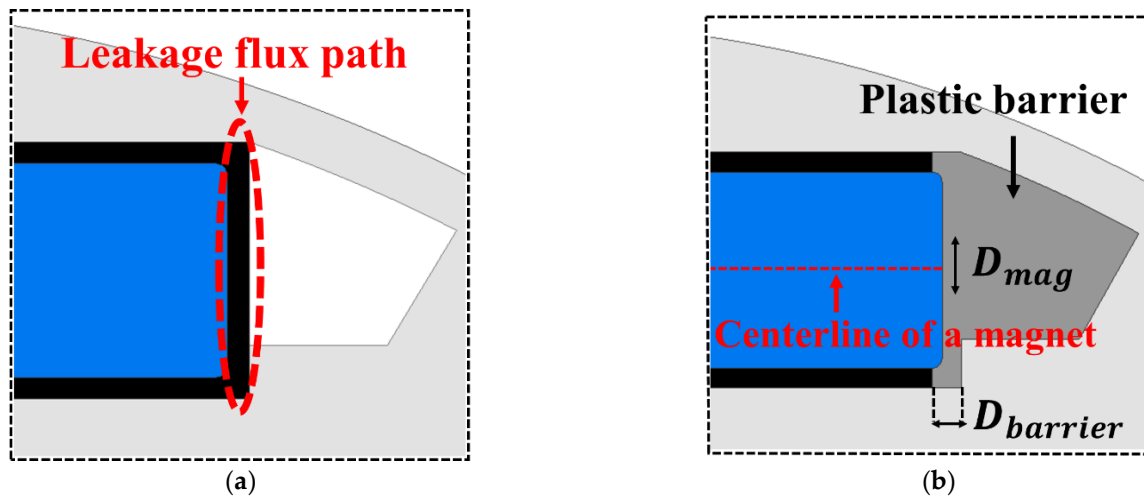


Figure 8. Setting of design variables: (a) leakage flux path; (b) design variables.

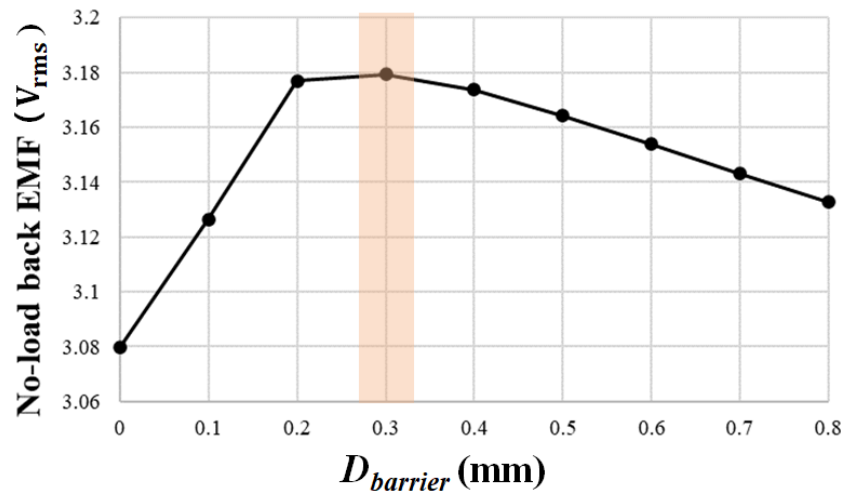


Figure 9. No-load back EMF variation with  $D_{barrier}$  (4000 rpm).

Figure 10 shows the no-load back EMF according to  $D_{mag}$  in the 0.3 mm  $D_{barrier}$  model with the maximum no-load back EMF. In Figure 10, the  $D_{mag}$  value of 0 mm means that the permanent magnet is located at the center of the insertion space in the rotor core. Increasing the  $D_{mag}$  value in the negative direction means that the permanent magnet moves toward the rotor center within the insertion space. Increasing the  $D_{mag}$  value in the positive direction means that the permanent magnet moves toward the airgap direction within the insertion space. Since the magnetic tolerance of the analysis model is 0.2 mm, it can be seen that the x-axis range in Figure 10 is from  $-0.2$  mm to  $0.2$  mm. Since the value of the no-load back EMF increases as the permanent magnet is positioned as close as possible to the airgap, it is important to select the maximum value of  $D_{mag}$ .

It was confirmed that the model with  $D_{barrier}$  of 0.3 mm and  $D_{mag}$  of 0.2 mm has the maximum no-load back EMF, and this was selected as the proposed model. Figure 11 shows the shape of the proposed model. The proposed model is advantageous in terms of manufacturability because the permanent magnet is attached in one direction within the insertion space of the rotor core.

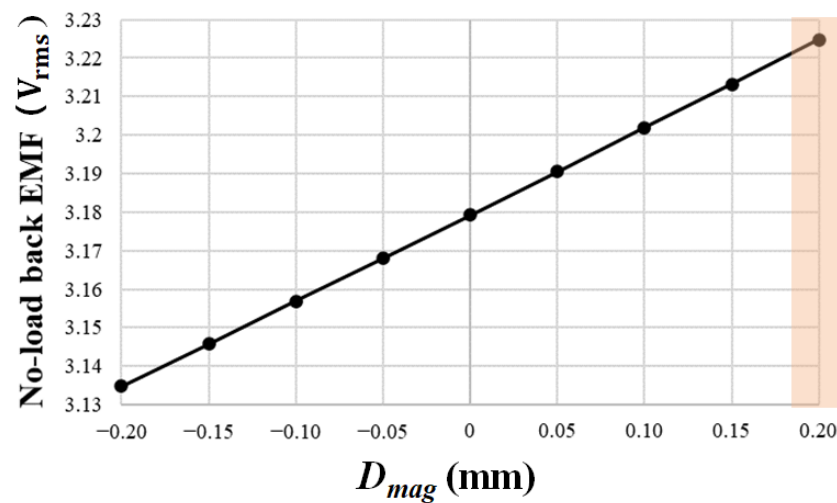


Figure 10. No-load back EMF variation with  $D_{mag}$  (4000 rpm).

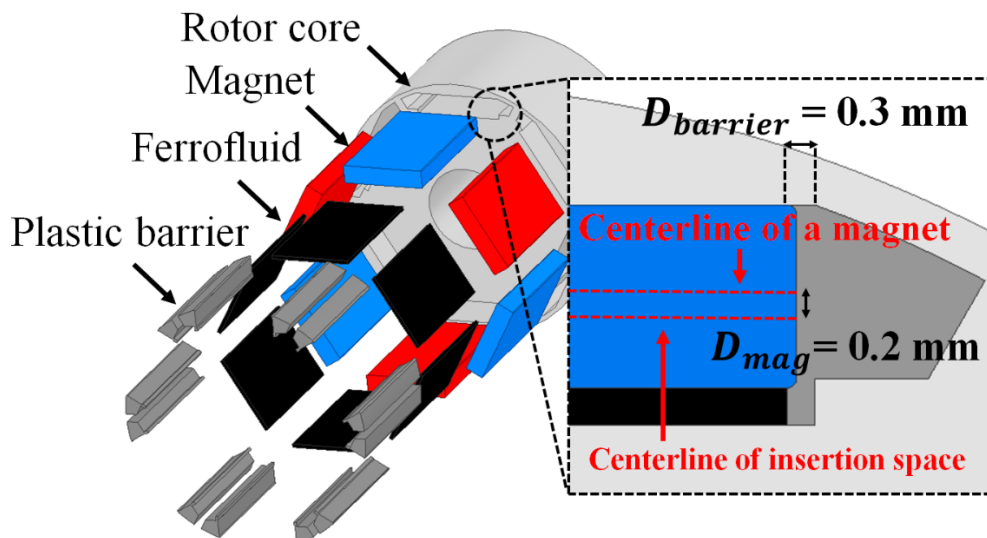


Figure 11. Rotor of the proposed model.

Figure 12 shows the waveforms of the no-load back EMF of the conventional and proposed models. Compared with the conventional model, the no-load back EMF of the proposed model increased by 17.95%.

Figure 13 shows the waveforms of their cogging torque. Cogging torque also increased by 161.72%. Therefore, in the next section, the design of the rotor to reduce the cogging torque is presented.

#### 4. Detailed Design of the Rotor to Reduce Cogging Torque

##### 4.1. Target Specification of IPMSM for the 4WD Hydraulic Control System

Injection of ferrofluid increases the no-load back EMF and performance of the torque, but it decreases the performance of the cogging torque and the torque ripple. Therefore, the proposed model needs an improved design for vibration and noise. In order to meet the target specifications of IPMSM in Table 2, the design of the rotor was performed. The torque, cogging torque, no-load line voltage total harmonic distortion (THD), efficiency, and torque ripple were selected as the target function.

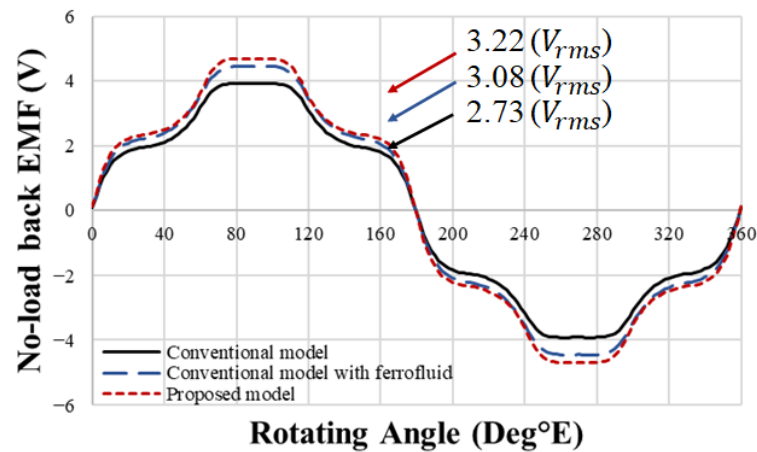


Figure 12. Comparison of the no-load back EMF (4000 rpm).

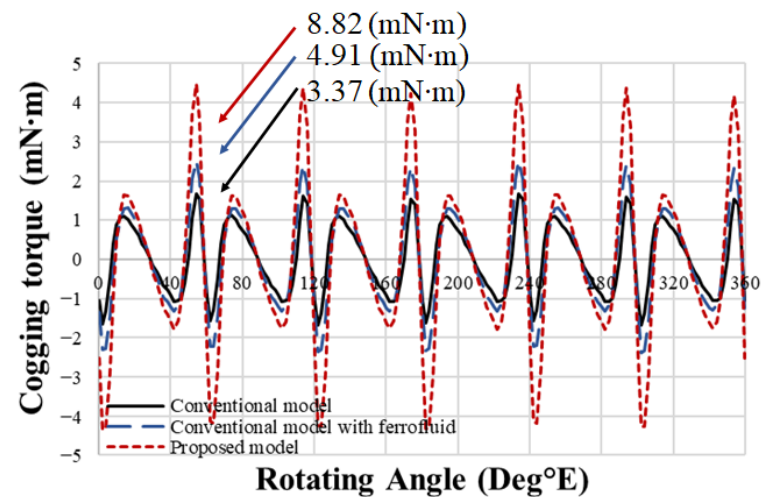


Figure 13. Comparison of the cogging torque (4000 rpm).

Table 2. Target specifications.

Parameter	Conventional Model	Proposed Model	Target Value	Unit
Torque (avg)	706.11	797.33	Max	mN·m
Cogging torque (pk2pk)	3.37	8.82	3	mN·m
No-load line Voltage THD	13.71	15.15	5	%
Efficiency	75.09	77.38	77.5	%
Torque ripple	14.88	16.57	5	%

#### 4.2. Variable of Rotor to Reduce Cogging Torque

The cogging torque is caused by the difference in the large reluctance between the permanent magnet and the stator slot and the low reluctance between the permanent magnet and the stator slot [23–26]. Tapering was applied to the outer diameter of the rotor to reduce the cogging torque by reducing the change in airgap reluctance [27–30]. The variable for tapering the outer diameter of the rotor was set as  $D_{tap}$ . As shown in Figure 14, the length of the rotor's radius is fixed, and tapering is greatly applied to the outer diameter of the rotor as the  $D_{tap}$  length increases.

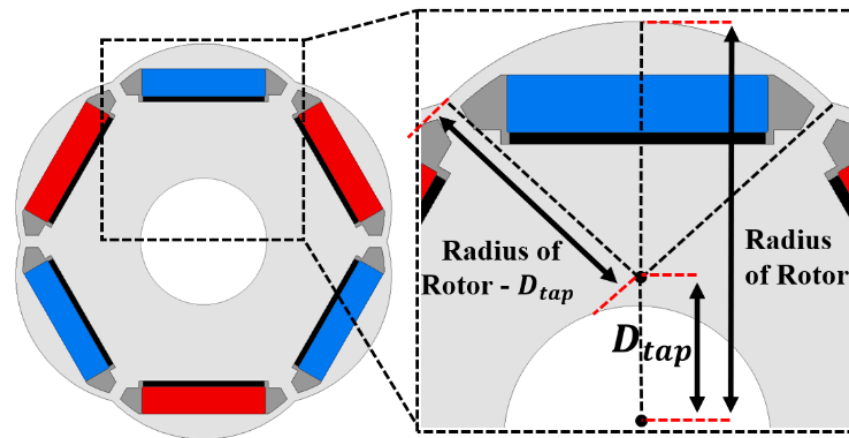


Figure 14. Variable  $D_{tap}$  for tapering the rotor.

#### 4.3. Analysis of Target Function

Figure 15 shows the change in torque and cogging torque according to the length of  $D_{tap}$ . As  $D_{tap}$  increases, the permanent magnet moves toward the rotor center and the torque decreases, and the rate of change in airgap reluctance and cogging torque decrease. However, when  $D_{tap}$  becomes greater than 4 mm, the cogging torque increases again.

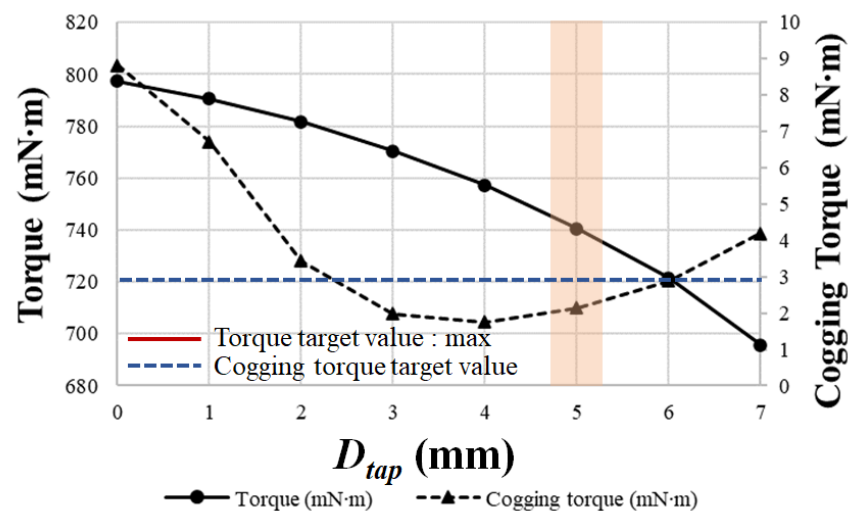


Figure 15. Torque and cogging torque variation with  $D_{tap}$  (4000 rpm).

Figure 16 shows the change in efficiency and no-load line voltage THD according to the length of  $D_{tap}$ . As  $D_{tap}$  increases, the iron loss and eddy current loss decrease, so the efficiency tends to increase. However, when the  $D_{tap}$  exceeds 4 mm, the efficiency decreases due to the decrease in the torque value.

Figure 17 shows the torque ripple according to the length of  $D_{tap}$ . As  $D_{tap}$  increases, the torque ripple also decreases, and it can be seen that  $D_{tap}$  values of 4 mm and 5 mm meet the target specification of less than 5%.

#### 4.4. Selection of the Final Model

A final model that satisfies the target specifications of IPMSM was derived through the design of the rotor that reduces the cogging torque and torque ripple of the proposed model. Table 3 shows the specifications of the final model. The final model is the shape of the proposed model with  $D_{tap}$  of 5 mm.

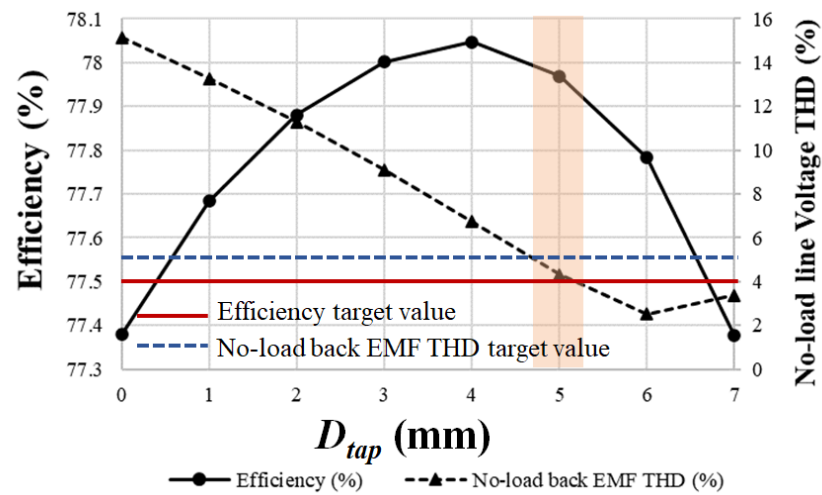


Figure 16. Efficiency and no-load line voltage total harmonic distortion (THD) with  $D_{tap}$  (4000 rpm).

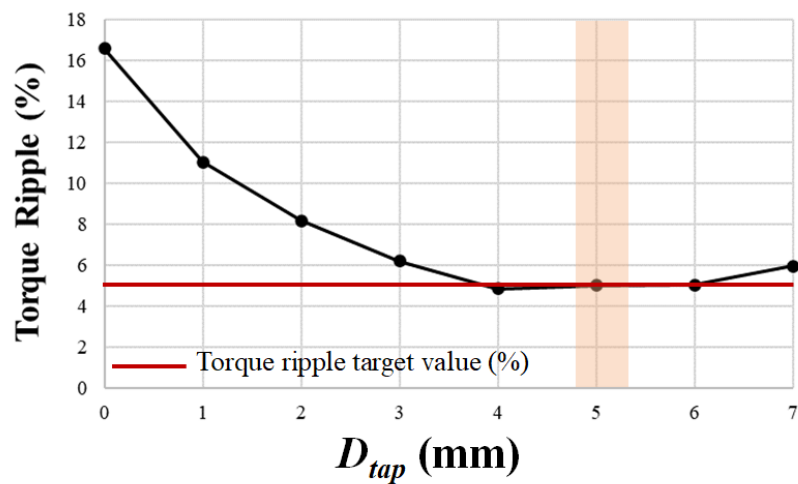
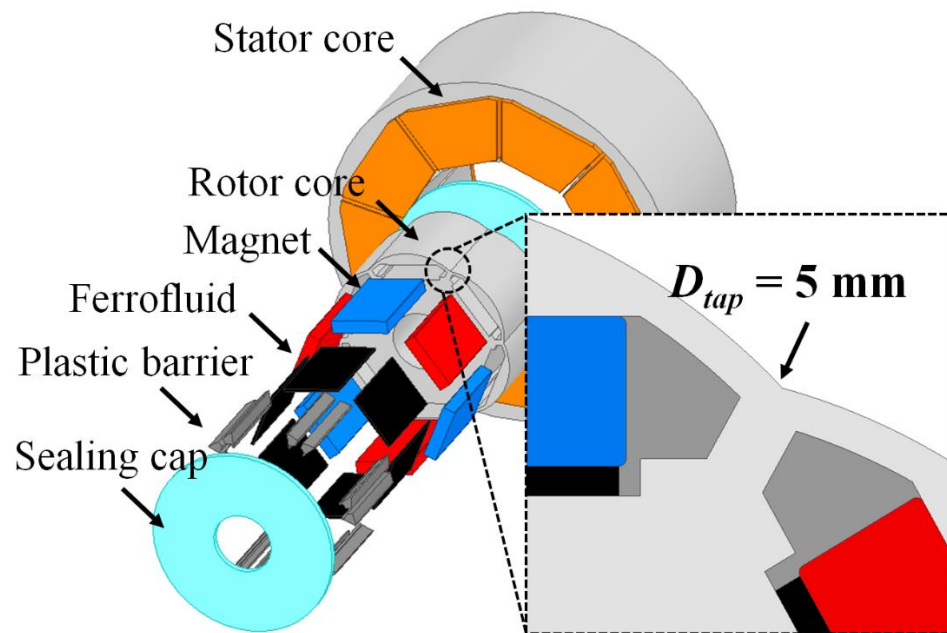


Figure 17. Torque ripple with  $D_{tap}$  (4000 rpm).

Table 3. Specification of the final model with ferrofluid.

Parameter	Conventional Model	Proposed Model	Final Model	Unit
Torque (avg)	706.11	797.33	740.58	mN·m
Cogging torque (pk2pk)	3.37	8.82	2.15	mN·m
No-load line voltage THD	13.71	15.15	4.32	%
Efficiency	75.09	77.38	77.96	%
Torque ripple	14.88	16.57	4.99	%

Figure 18 shows the rotor when ferrofluid is injected into the final model. In Figure 18, the sealing cap is fixed to the rotor core with a bond and plays the role of preventing ferrofluid from leaking out to the airgap.



**Figure 18.** The final model injected with ferrofluid.

#### 4.5. Structural FEA

When tapering is applied to the rotor, it is important to confirm the structural strength of the rib. Therefore, the equivalent stress and safety factor of the conventional model and the final model were compared through structural FEA. Figure 19 shows the equivalent stress when the rotor rotates counterclockwise at a speed of 4000 rpm. Since the rotor rotates counterclockwise, it can be seen that the permanent magnet sticks clockwise in the insertion space. The max equivalent stress of the conventional model occurred at the edge of the permanent magnet that meets the support structure of the rotor core and had a value of about 8.62 MPa. In the case of the final model, in contrast, the permanent magnet was stably fixed due to the plastic barrier structure and had a value of about 1.78 MPa. The equivalent stress of the rib was 1.90 MPa for the conventional model and 1.61 MPa for the final model, indicating that the final model had a slightly smaller value. This is because the burden on the ribs is also reduced through the plastic barrier. In addition, when tapering the rotor, the thickness of the rib was designed to be constant, so it can be confirmed that there is no significant difference in structural strength.

Figure 20 shows the safety factors of the conventional and final models. Like the previous analysis, the safety factor was compared when the rotor rotated counterclockwise at a speed of 4000 rpm. At the corner of the permanent magnet, which is the point of maximum equivalent stress of the conventional model, it can be confirmed that the safety factor has a value of 9.28, which is the lowest. At other points, both the safety factors of the conventional and final models have values of 15, which are the same. Therefore, it is finally confirmed that there is no problem in the structural strength of the final model compared to that of the conventional model.

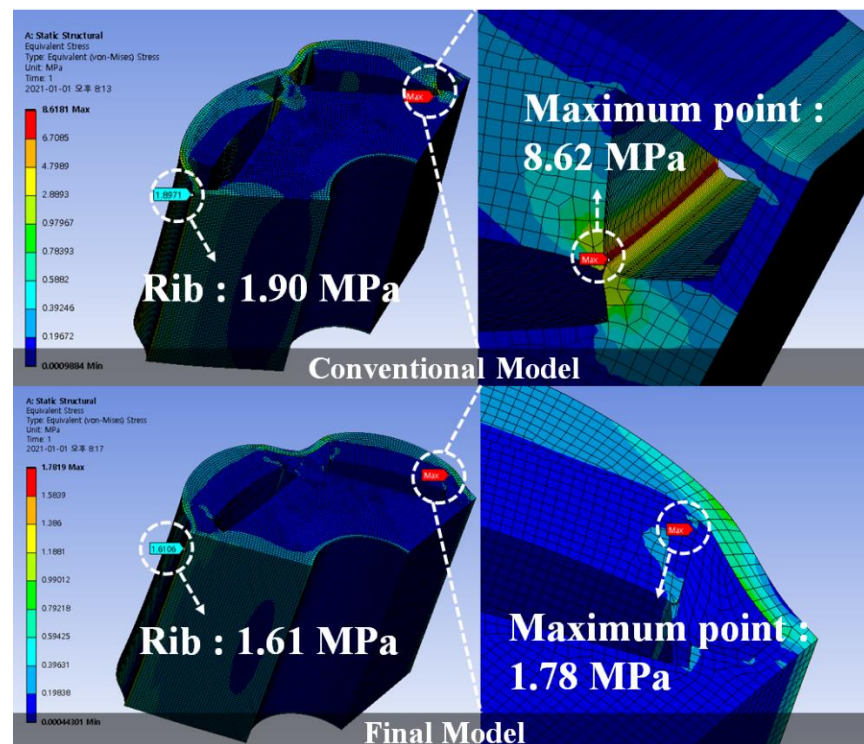


Figure 19. Comparison of the equivalent stress (4000 rpm).

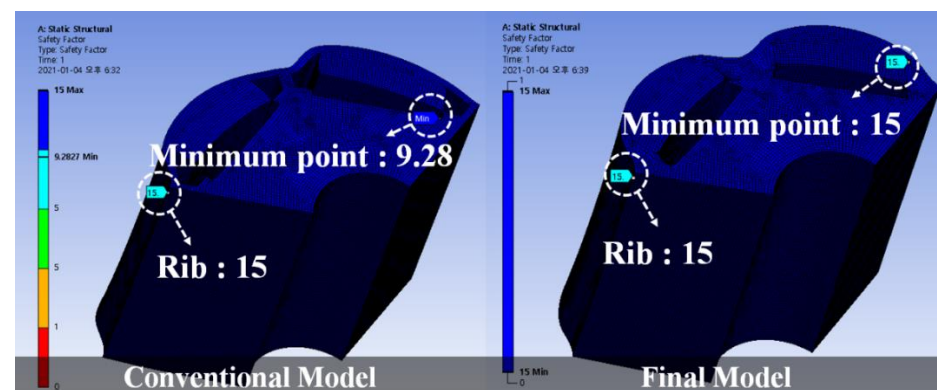


Figure 20. Comparison of the safety factor (4000 rpm).

## 5. Test and Verification

A prototype of the final model was prepared, and value of the no-load line voltage was checked according to whether or not ferrofluid was injected. The process of setting up the experimental equipment is shown in Figure 21. First, a permanent magnet was inserted into the rotor core. The permanent magnet was inserted to adhere to the airgap in the insertion space, as shown in Figure 18. Next, plastic barriers made by 3D printing were inserted into both ends of the permanent magnet in the insertion space to fix the magnet. When ferrofluid is sprayed onto a permanent magnet through a syringe, the ferrofluid is sucked into the magnet tolerance due to the magnetism of the permanent magnet. Ferrofluid was injected until it was sufficiently injected into the insertion space and was no longer sucked into the magnetic tolerance. The capacity of the ferrofluid and the volume of the rotor and permanent magnet used to make the final model are shown in Table 4. Lastly, when the plastic sealing cap is attached to both ends of the z-axis of the rotor core with a bond as in Figure 18, the leakage of ferrofluid can be prevented.



Figure 21. Process of setting up the experimental equipment.

Table 4. Capacity of ferrofluid used to make the final model.

Parameter	Value	Unit
Volume of rotor	100,399	mm <sup>3</sup>
Volume of permanent magnet	4145	mm <sup>3</sup>
Capacity of ferrofluid	0.812	mL

Figure 22 shows the dynamo test result of no-load line voltage at a rotation speed of 572 rpm. Since the test was performed with and without the injection of ferrofluid, it can be seen that two waveforms appear.

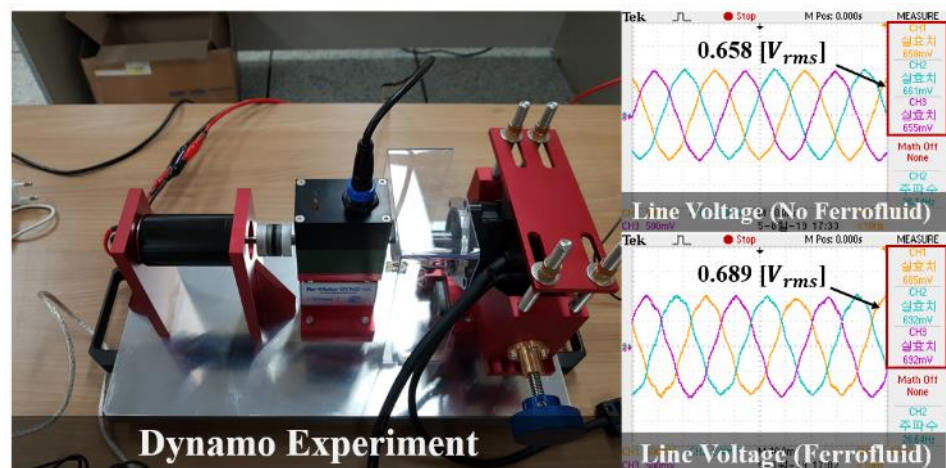
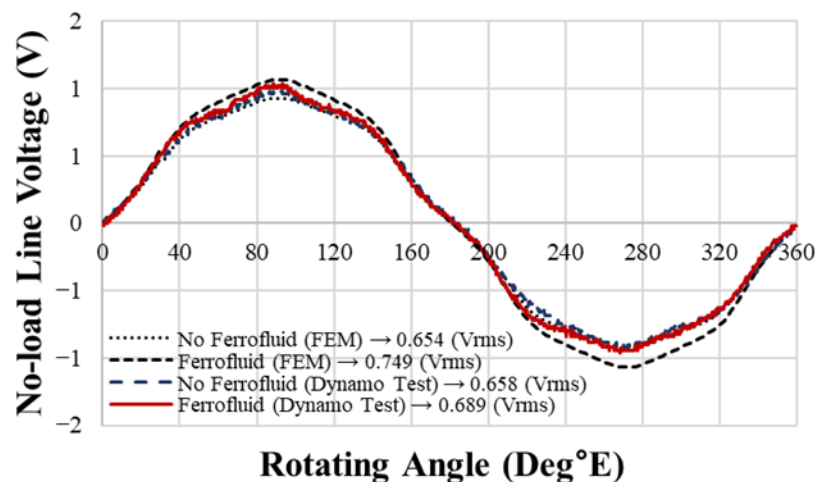


Figure 22. Dynamo experiment and results (572 rpm).

The values of no-load line voltage from the dynamo test and FEA simulation can be compared in Figure 23. The value of the no-load line voltage of the final model injected with ferrofluid increased by 14.53% in the FEA simulation compared to the model without ferrofluid. In the dynamo test, however, an increase of 4.71% can be seen. The cause of this can be thought as the limitation of 3D printing technology. In small motors, the plastic barrier that enters the insertion space of the rotor core is small, so it is difficult to fully print it by 3D printing. Therefore, when there is a gap in the barrier part, the ferrofluid gathers in the path where the reluctance is minimized, which forms a leakage flux path, as shown in Figure 8a. Research to supplement this will be conducted in a future study. The tolerance was made large by making a plastic barrier with a 3D printer, but it is believed that tolerance and errors can be reduced by making it with a plastic injection mold.



**Figure 23.** No-load line voltage of the final model through a dynamo experiment and finite element analysis (FEA) simulation (572 rpm).

In Table 4, it can be seen that the no-load line voltage was improved by 4.71% while using very little ferrofluid compared to the total volume of the rotor. The increase in the volume of the magnet that was necessary to achieve the increase in EMF obtained through ferrofluid was confirmed. According to the thickness of the permanent magnet, the no-load line voltage was analyzed at 572 rpm through FEA simulation. It can be seen in Figure 24 that the thickness of the permanent magnet has to be increased from the existing 2 mm to 2.3 mm. This means that the use of permanent magnets should be increased by 15%.

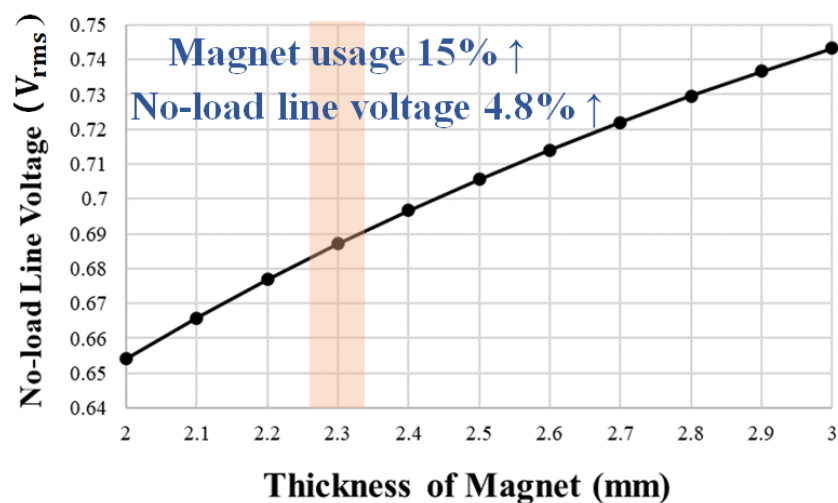


**Figure 24.** No-load line voltage according to the thickness of the magnet in the final model (no ferrofluid, 572 rpm).

## 6. Conclusions

In this paper, a method to improve the performance of the no-load back EMF and magnetic torque by injecting ferrofluid into the magnet tolerance is proposed. Since ferrofluid is injected into the magnet tolerance instead of adhesive, a new rotor configuration is proposed to fix the magnet. The new rotor configuration through a plastic barrier prevents the ferrofluid from acting as a leakage path and fixes a permanent magnet, which derives a model with the maximum no-load back EMF. The final model was actually produced, and a dynamo test was conducted. The increase in the no-load line voltage was confirmed through ferrofluid injection.

The method of improving the torque density through ferrofluid proposed in this study can be expected to improve the performance without a large cost compared to previous

studies. Previous studies have focused on injecting ferrofluid into the airgap. In this case, however, a large amount of ferrofluid was needed, and it increased the cost. Fabrication was also disadvantageous because the performance varied depending on the viscosity of the ferrofluid, and sealing was difficult. The design of the shape in this study can complement the shortcomings of previous studies. The shape of the rotor suggested in this study is considered to be useful in fields that require high performance and high efficiency, such as robots, aviation, and medical fields.

**Author Contributions:** Conceptualization, K.-S.K. and W.-H.K.; methodology, I.-J.Y.; software, I.-J.Y.; validation, I.-J.Y.; formal analysis, I.-J.Y.; investigation, I.-J.Y.; resources, I.-J.Y.; data curation, I.-J.Y.; writing—original draft preparation, I.-J.Y.; writing—review and editing, S.-W.S. and D.-H.K.; visualization, S.-W.S. and D.-H.K.; supervision, W.-H.K. All authors have read and agreed to the published version of the manuscript.

**Funding:** This work was supported by the National Research Foundation of Korea (NRF) Grant funded by the Korea government (MSIP; Ministry of Science, ICT & Future Planning) (No. NRF-2018R1C1B5085711) and in part by the National Research Foundation of Korea (NRF) Grant funded by the Korean Government (MSIT) under grant 2020R1A2C1013724 and in part by the Gachon University Research Fund of 2019 under grant GCU-2019-0770.

**Institutional Review Board Statement:** Not applicable.

**Informed Consent Statement:** Not applicable.

**Data Availability Statement:** Not applicable.

**Acknowledgments:** Not applicable.

**Conflicts of Interest:** The authors declare no conflict of interest.

## References

1. Park, T.H.; Kim, J.-H.; Seo, S. Facile and rapid method for fabricating liquid metal electrodes with highly precise patterns via one-step coating. *J. Adv. Funct. Mater.* **2020**, *30*, 2003694. [[CrossRef](#)]
2. Yang, Y.Y.; Han, J.; Huang, J.; Sun, J.; Wang, Z.L.; Seo, S.; Sun, Q. Stretchable energy-harvesting tactile interactive interface with liquid-metal-nanoparticle-based electrodes. *J. Adv. Funct. Mater.* **2020**, *30*, 1909652. [[CrossRef](#)]
3. Kim, J.H.; Seo, S. Fabrication of an imperceptible liquid metal electrode for triboelectric nanogenerator based on gallium alloys by contact printing. *J. Appl. Surf. Sci.* **2020**, *509*, 145353. [[CrossRef](#)]
4. Cho, H.; Kim, J.; Suga, K.; Ishigami, T.; Park, H.; Bang, J.W.; Seo, S.; Choi, M.; Chang, P.-S.; Umakoshi, H.; et al. Microfluidic platforms with monolithically integrated hierarchical apertures for the facile and rapid formation of cargo-carrying vesicles. *J. R. Soc. Chem.* **2015**, *15*, 373–377. [[CrossRef](#)]
5. Kwon, U.; Kim, B.-G.; Nguyen, D.C.; Park, J.-H.; Ha, N.Y.; Kim, S.-J.; Ko, S.H.; Lee, S.; Lee, D.; Park, H.J. Solution-processible crystalline NiO nanoparticles for high-performance planar perovskite photovoltaic cells. *J. Sci. Rep.* **2016**, *6*, 1–10. [[CrossRef](#)] [[PubMed](#)]
6. Lee, D.; Paeng, D.; Park, H.K.; Grigoropoulos, C.P. Vacuum-free, maskless patterning of Ni electrodes by laser reductive sintering of NiO nanoparticle ink and its application to transparent conductors. *J. ACS Nano* **2014**, *8*, 9807–9814. [[CrossRef](#)] [[PubMed](#)]
7. Baek, S.-D.; Biswas, P.; Kim, J.-W.; Kim, Y.C.; Lee, T.I.; Myoung, J.-M. Low-temperature facile synthesis of Sb-doped p-type ZnO nanodisks and its application in homojunction light-emitting diode. *J. ACS Appl. Mater. Interfaces* **2016**, *8*, 13018–13026. [[CrossRef](#)]
8. Kim, J.-W.; Lee, S.J.; Biswas, P.; Lee, T.I.; Myoung, J.-M. Solution-processed n-ZnO nanorod/p-Co<sub>3</sub>O<sub>4</sub> nanoplate heterojunction light-emitting diode. *J. Appl. Surf. Sci.* **2017**, *406*, 192–198. [[CrossRef](#)]
9. Islam, S.; Zubair, M.; Tassaddiq, A.; Shah, Z.; Alrabaiah, H.; Kumam, P.; Khan, W. Unsteady Ferrofluid Slip Flow in the Presence of Magnetic Dipole with Convective Boundary Conditions. *IEEE Access* **2020**, *8*, 138551–138562. [[CrossRef](#)]
10. Ivanov, A.O.; Kuznetsova, O.B. Magnetic properties of dense ferrofluids. *J. Magn. Magn. Mater.* **2002**, *252*, 135–137. [[CrossRef](#)]
11. Gautam, N.; Thirupathi, G.; Singh, R. Magnetoviscosity of paraffin-based barium ferrite ferrofluid. *IEEE Trans. Magn.* **2016**, *52*, 1–4. [[CrossRef](#)]
12. Thirupathi, G.; Singh, R. Study of magnetoviscosity of ferromagnetic MnZn-ferrite ferrofluid. *IEEE Trans. Magn.* **2015**, *51*, 3–6. [[CrossRef](#)]
13. Clark, N.A. Ferromagnetic ferrofluids. *Nature* **2013**, *504*, 229–230. [[CrossRef](#)] [[PubMed](#)]
14. Santiago-Quinones, D.I.; Raj, K.; Rinaldi, C. A comparison of the magnetorheology of two ferrofluids with different magnetic field-dependent chaining behavior. *Rheol. Acta.* **2013**, *52*, 719–726. [[CrossRef](#)]
15. Klokkenburg, M.; Ern , B.H. Comparison of reversible and irreversible dipolar assemblies in a ferrofluid. *J. Magn. Magn. Mater.* **2006**, *306*, 85–91. [[CrossRef](#)]

16. Lin, J.-F.; Sheu, J.-J.; Lee, M.-Z.; Lin, Y.-Q. Linear birefringence and dichroism measurements for silica coated iron oxide ferrofluids. *IEEE Trans. Magn.* **2014**, *50*, 18–21. [[CrossRef](#)]
17. Yang, I.-J.; Lee, S.-H.; Kim, D.-H.; Kim, K.-S.; Jang, I.-S.; Kim, W.-H. Improvement in torque density by ferrofluid Injection into interior permanent magnet synchronous motor. In Proceedings of the 2020 IEEE Energy Conversion Congress and Exposition (ECCE), Detroit, MI, USA, 11–15 October 2020; pp. 1364–1370.
18. Nethe, A.; Scholz, T.; Stahlmann, H.D.; Filtz, M. Ferrofluids in electric motors—A numerical process model. *IEEE Trans. Magn.* **2002**, *38*, 1177–1180. [[CrossRef](#)]
19. Engelmann, S.; Nethe, A.; Scholz, T.; Stahlmann, H.D. Concept of a new type of electric machines using ferrofluids. *J. Magn. Magn. Mater.* **2005**, *293*, 685–689. [[CrossRef](#)]
20. Engelmann, S.; Nethe, A.; Scholz, T.; Stahlmann, H.D. Force enhancement on a ferrofluid-driven linear stepping motor model. *J. Magn. Magn. Mater.* **2004**, *272–276*, 2345–2347. [[CrossRef](#)]
21. Zeng, G.; Xiang-yu, Y.; Yin, H.; Zhao, S.; Cao, J.; Qiu, L. Asynchronous machine with ferrofluid in gap: Modeling, simulation, and analysis. *IEEE Trans. Magn.* **2020**, *56*, 55–58. [[CrossRef](#)]
22. Hanselman, D. *Brushless Permanent Magnet Motor Design*, 2nd ed.; E-Man Press LLC: Orono, ME, USA, 2006; pp. 133–139.
23. Li, T.; Slemon, G. Reduction of cogging torque in permanent magnet motors. *IEEE Trans. Magn.* **1988**, *24*, 2901–2903.
24. Keyhani, A.; Studer, C.; Sebastian, T.; Murthy, S.K. Study of cogging torque in permanent magnet machines. *Electr. Mach. Power Syst.* **1999**, *27*, 665–678. [[CrossRef](#)]
25. Dosiek, L.; Pillay, P. Cogging torque reduction in permanent magnet machines. *IEEE Trans. Ind. Appl.* **2007**, *43*, 1565–1571. [[CrossRef](#)]
26. Zhu, Z.Q.; Howe, D. Influence of design parameters on cogging torque in permanent magnet machines. *IEEE Trans. Energy Convers.* **2000**, *15*, 407–412. [[CrossRef](#)]
27. Jung, Y.-H.; Lim, M.-S.; Yoon, M.-H.; Jeong, J.-S.; Hong, J.-P. Torque ripple reduction of IPMSM applying asymmetric rotor shape under certain load condition. *IEEE Trans. Energy Convers.* **2018**, *33*, 333–340. [[CrossRef](#)]
28. Jung, Y.-H.; Park, M.-R.; Lim, M.-S. Asymmetric rotor design of IPMSM for vibration reduction under certain load condition. *IEEE Trans. Energy Convers.* **2020**, *35*, 928–937. [[CrossRef](#)]
29. Evans, S.A. Salient pole shoe shapes of interior permanent magnet synchronous machines. In Proceedings of the 19th International Conference on Electrical Machines, Rome, Italy, 6–8 September 2010.
30. Jang, I.-S.; Kim, W.-H. Study on Electromagnetic Vibration Analysis Process for PM Motors. *IEEE Trans. Appl. Supercond.* **2020**, *30*. [[CrossRef](#)]